

Efficient Functional Delivery of siRNA using Mesoporous Silica Nanoparticles with Ultralarge Pores

Hee-Kyung Na, Mi-Hee Kim, Kihyun Park, Soo-Ryoon Ryoo, Kyung Eun Lee, Hyesung Jeon, Ryong Ryoo, Changbong Hyeon, and Dal-Hee Min*

Among various nanoparticles, mesoporous silica nanoparticles (MSNs) have attracted extensive attention for developing efficient drug-delivery systems, mostly due to their high porosity and biocompatibility. However, due to the small pore size, generally below 5 nm in diameter, potential drugs that are loaded into the pore have been limited to small molecules. Herein, a small interfering RNA (siRNA) delivery strategy based on MSNs possessing pores with an average diameter of 23 nm is presented. The siRNA is regarded as a powerful gene therapeutic agent for treatment of a wide range of diseases by enabling post-transcriptional gene silencing, so-called RNA interference. Highly efficient, sequence-specific, and technically very simple target gene knockdown is demonstrated using MSNs with ultralarge pores of size 23 nm *in vitro* and *in vivo* without notable cytotoxicity.

1. Introduction

RNA interference (RNAi) is a conserved gene silencing mechanism in eukaryotic cells, where targeted cleavage of messenger RNA (mRNA) is achieved for regulation of undesired gene expression.^[1] Since the discovery of RNAi in *Caenorhabditis elegans* by Fire, Mello, and co-workers in 1998,^[2] it has been extensively investigated to solve

fundamental biological questions^[3] and for applications in the biomedical area.^[4] In particular, RNAi is thought to provide enormous opportunity as an alternative therapeutic for diseases formerly considered not treatable with conventional small-molecule-based drugs.^[5]

The RNAi pathway can be triggered by introduction of exogenous small interfering RNA (siRNA) to the cytoplasm of eukaryotes.^[1] Exogenous synthetic siRNA usually consists of 21–23 nucleotides (nt) with 2–3 nt overhangs at the 3'-position. siRNA holds promise as a powerful gene therapeutic agent for treatment of a wide range of diseases from viral infection^[6] to cancer^[7]—theoretically all of the diseases caused by upregulation of an aberrant gene—by utilizing endogenous RNAi machinery in mammalian cells. Although siRNA has shown significant potential as a new gene therapy, difficulty in delivery of an effective dose of therapeutic siRNAs while maintaining intact chemical structure into target cells with high gene silencing efficacy hindered advancement of siRNA as a new therapeutic and expansion of siRNA in more practical, routine applications. siRNA possesses a polyanionic character and permeation of siRNA across lipid bilayers is known to be negligible without assistance.^[8] In addition, exogenous siRNA undergoes degradation upon exposure to nucleases in biological systems.

To date, viral gene,^[9] recombinant protein,^[10] liposomes,^[11] cationic polymers,^[12] and various types of nanoparticles and nanomaterials^[13–17] have been exploited for

H.-K. Na, M.-H. Kim, S.-R. Ryoo, Prof. R. Ryoo
Department of Chemistry
KAIST, Daejeon 305-701, Korea

Dr. K. Park, Prof. C. Hyeon
School of Computational Sciences
Korea Institute for Advanced Study
Seoul 130-722, Korea

Dr. K. E. Lee, Dr. H. Jeon
Biomedical Research Center
Korea Institute of Science and Technology
Seoul 136-791, Korea

Prof. D.-H. Min
Department of Chemistry
Seoul National University
Seoul 151-747, Korea
E-mail: dalheemin@snu.ac.kr



DOI: 10.1002/sml.201200028

delivery of siRNAs into mammalian cells. Many cationic liposomes and polymers are considered too cytotoxic for clinical application.^[18] Chemical modification of the siRNA backbone has also been employed for obtaining stable and membrane-permeable siRNA.^[19] However, due to high cost, the time-consuming process, and labor intensiveness, it may not be amenable for use in clinical application. A significant effort has been made to realize an efficient drug-delivery system (DDS) using various types of nanoparticles, including quantum dots,^[13] magnetic particles,^[14] silica nanoparticles,^[15,16] and gold nanoparticles.^[17] Among them, mesoporous silica nanoparticles (MSNs) have been harnessed as a promising drug-delivery vehicle for anticancer drugs, such as doxorubicin and paclitaxel, due to their tunable pore and particle size, high surface area, large pore volume, ease of surface functionalization, and high biocompatibility.^[20] In addition, a controlled and sustained release system has been demonstrated, which may be applicable to many different types of drugs, by loading small-molecule drugs into the pore with stimuli-responsive gate opening/closing systems.^[21–23] In contrast, biomacromolecules, such as protein, DNA, and RNA, have been immobilized or adsorbed mostly on the outer surface of the mesoporous silica instead of encapsulated inside MSN pores, due to the relatively small pore size of MSNs in order to hold such biomacromolecules inside, thus making them vulnerable to enzyme-mediated degradation *in vivo*.^[15,24–26]

Herein, we report a highly efficient siRNA delivery system based on MSNs with large pores of diameter 23 nm (MSN23). The MSN23 is prepared by a simple procedure for expansion of small pores by treatment of the conventional MSN possessing small pores (≈ 2 nm in diameter) with trimethylbenzene.^[27] Loading of siRNA was then achieved by simply mixing siRNAs with the amine-functionalized MSN23. The siRNAs were expected to be loaded into MSN pores, thereby enabling cellular delivery of siRNA while maintaining its chemical integrity even in the presence of serum proteins (**Figure 1**). The process of siRNA loading and the interaction

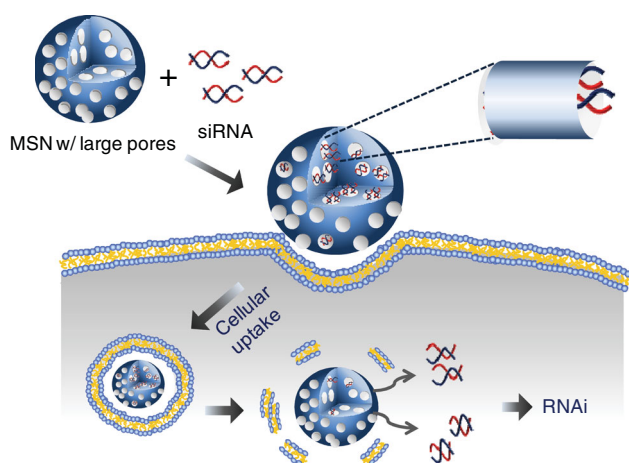


Figure 1. The siRNA delivery system with a silica nanoparticle possessing large pores. The siRNA delivery vehicle is designed to load siRNA molecules inside the pores for high loading capacity and protection from nucleases, to finally accomplish efficient siRNA-mediated RNAi.

of siRNAs with pores were further studied by various experiments and theoretical calculations. The validity of the siRNA delivery system was demonstrated using two different siRNAs targeting a model gene—green fluorescent protein (GFP)—and a therapeutically relevant gene—vascular endothelial growth factor (VEGF)—*in vitro* and *in vivo*. The present delivery system showed higher gene silencing efficiency than a commercially available gene transfection reagent, Lipofectamine 2000, with much lower cytotoxicity.

2. Results and Discussion

To prepare MSN23, we employed a pore expansion strategy with MSN with 2 nm pores (MSN2) using trimethylbenzene (TMB) as a swelling agent.^[27] We first synthesized MSN2 according to a previously reported method.^[28] MSN23 was synthesized by addition of TMB and distilled water (1:1, v/v) to the ethanolic solution of MSN2, followed by incubation for 4 days at 140 °C in an autoclave. Successful preparation of MSN23 was confirmed by transmission electron microscopy (TEM) and a nitrogen sorption experiment (**Figure 2**). Both MSN2 and MSN23 showed narrow size distribution, about 200 nm in diameter, in TEM (Figure 2a,b) and scanning electron microscopy (SEM; Figure S1, Supporting Information) images. Monodispersity of nanomaterials is essential in the design of a well-defined DDS, since the size of nanoparticles, in addition to shape and surface chemistry, is one of the factors to determine cellular uptake and further efficacy of the DDS. TEM images of MSN23 showed rather rough surfaces with many large pores, compared with MSN2. It is notable that MSN23 exhibited high monodispersity even after pore expansion, for which the preparation method is straightforward and allows for large-scale synthesis (at least 1 g at a time using a laboratory setup). Further physical characterization of pore size, surface area, and pore volume of MSNs was carried out by nitrogen sorption experiments (Figure 2c, Figure S2). Pore size distribution, which was calculated according to the Barrett–Joyner–Halenda (BJH) method, revealed average pore sizes of 2.2 and 23 nm for MSN2 and MSN23, respectively. The surface area of MSNs obtained using the Brunauer–Emmett–Teller (BET) method was decreased as expected from 1337 to 395 m² g⁻¹ by expansion of the pores.

Next, MSN2 and MSN23 were aminated for the presentation of positive charges on their inner and outer surfaces under physiological conditions by grafting 3-aminopropyltriethoxysilane (APTES), so that negatively charged siRNA can be adsorbed via electrostatic interaction. The degree of amination determined by measurement of relative amounts of nitrogen and carbon through elemental analysis revealed that both MSN2 and MSN23 possess a similar amount of amines per gram, 3.6 mmol g⁻¹. An imaging dye was then conjugated onto the MSN surface by reaction of surface amine groups with *N*-hydroxysuccinimide (NHS)-activated carboxytetramethylrhodamine (TAMRA) to enable tracking of the MSNs (TAMRA-conjugated MSN, T-MSN) in mammalian cells using a fluorescence microscope. Polyethylene glycol (PEG, molecular weight (MW) 5000) was next conjugated to MSNs (PEGylated T-MSN, P-T-MSN) to minimize agglomeration

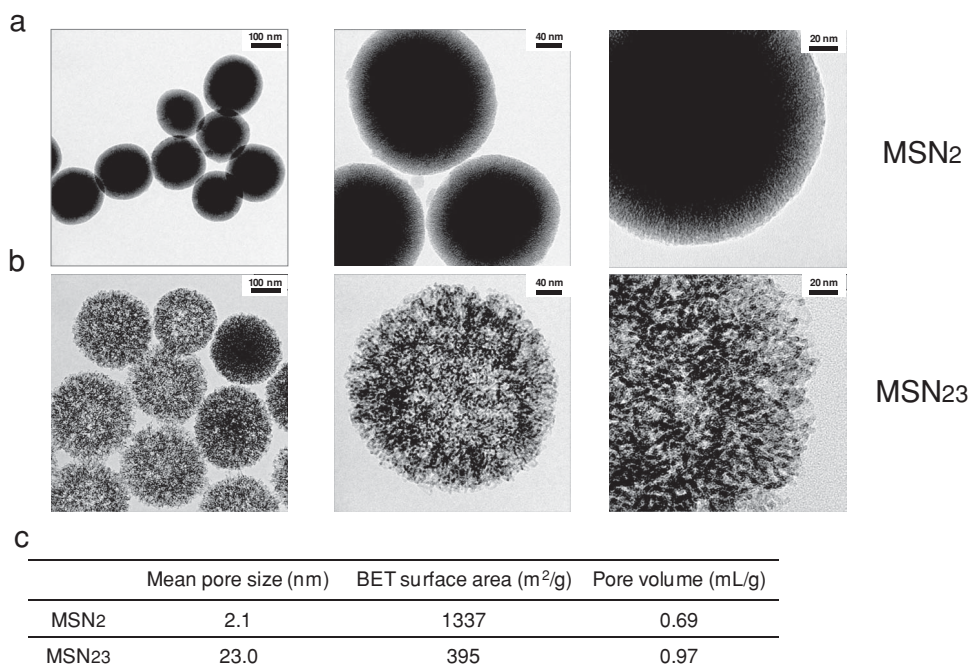


Figure 2. Physical characterization of the prepared silica nanoparticles. TEM images of a) MSN2 and b) MSN23. c) Mean pore size, surface area, and pore volumes obtained by a nitrogen sorption experiment.

of the particles and nonspecific adsorption of biomolecules, such as serum proteins. Then, siRNA against GFP (siGFP) was loaded onto each particle by incubation of the particles (20 μg) with siRNA (25 pmol) in phosphate-buffered saline (PBS, pH 7.4) for 1 h at room temperature. Adsorption of siRNA onto the particles and loading capacity were characterized by measurement of zeta potential and by gel electrophoresis (Figure 3a, Figure S3). We intended to compare P-T-MSN23 and P-T-MSN2 for siRNA loading capacity but gel electrophoresis revealed that loading of siRNA to P-T-MSN2 was negligible (data not shown). The result suggests that adsorption of siRNA onto the surface of MSNs, not into the pores, may be greatly reduced after PEGylation of the particles. Due to very limited siRNA loading capacity of P-T-MSN2, T-MSN2 was used instead of P-T-MSN2 for comparison throughout the present study. The zeta potential of T-MSN2 changed from 8.1 to -6.49 mV after siRNA loading, whereas the change was from 19.4 to 2.54 mV for P-T-MSN23, thereby indicating that P-T-MSN23, unlike T-MSN2, maintains a positive zeta potential value even after loading of negatively charged siRNA. The loading capacity of each particle for siRNA was calculated by measurement of the relative intensity of bands corresponding to unbound siRNA appearing in a gel after electrophoresis (Figure S3). P-T-MSN23-siRNA complex afforded about two times higher siRNA loading capacity (1.25 pmol μg^{-1} , number of siRNA per particle: 5800) than T-MSN2-siRNA (0.55 pmol μg^{-1} , number of siRNA per particle: 2550), thus implying that P-T-MSN23 is more favorable than T-MSN2 as a siRNA delivery system.

Next, we investigated the physicochemical basis of differences in zeta potentials of MSNs and loading of siRNAs

(Figure 3b–d). Since siRNA and amine-functionalized MSNs are oppositely charged, electrostatic attraction should be one of the main driving forces in loading of siRNA onto MSNs. The zeta potential, which characterizes the screened electrostatic potential of MSNs in a dispersed medium, is expected to be proportional to the effective surface charge density of MSNs. The effective surface area of MSN2 is estimated as higher (outer surface area (0.14 μm^2) + pore surface area (17 μm^2) \approx 17.1 μm^2) than that of MSN23 (outer surface area (0.17 μm^2) + pore surface area (2.7 μm^2) \approx 2.9 μm^2) and the amine contents of MSN2 and MSN23 per gram are similar. For 42-nt siRNA that has a negative effective charge (Z_{eff}) on phosphate groups, free energy stabilization due to adsorption of a siRNA molecule to MSN is $\epsilon_{\text{int}} = -Z_{\text{eff}}e\zeta$, where e is the elementary charge ($e \approx 1.602 \times 10^{-19}$ C) and ζ is the zeta potential. Calculations were performed assuming that the particles are not modified with TAMRA or PEG. Detailed electric potential evaluated by solving the Poisson–Boltzmann equation shows that the value of potential for the MSN2 is larger inside the pore than on the outer surface. The relative difference of the electric potential inside and outside the pore increases as the pore size decreases. The screening of the amine charge by the counter ions is not effective if R_p becomes comparable to or smaller than the Debye screening length, as in MSN2 ($R_p = 1.05$ nm \approx $\kappa^{-1} \approx 1$ nm; Figure 3b–d, Supporting Information). Despite the strong electric field toward the pore, the pore radius, which is smaller than the size of a siRNA molecule (radius of gyration for siRNA, R_G , with $R_p < R_G \approx 2.0$ nm), prevents entry of siRNAs into the pore. In contrast, for MSN23, the pore size of which is greater than siRNA ($R_G < R_p$), siRNAs can move freely into the pore and stick to the pore wall

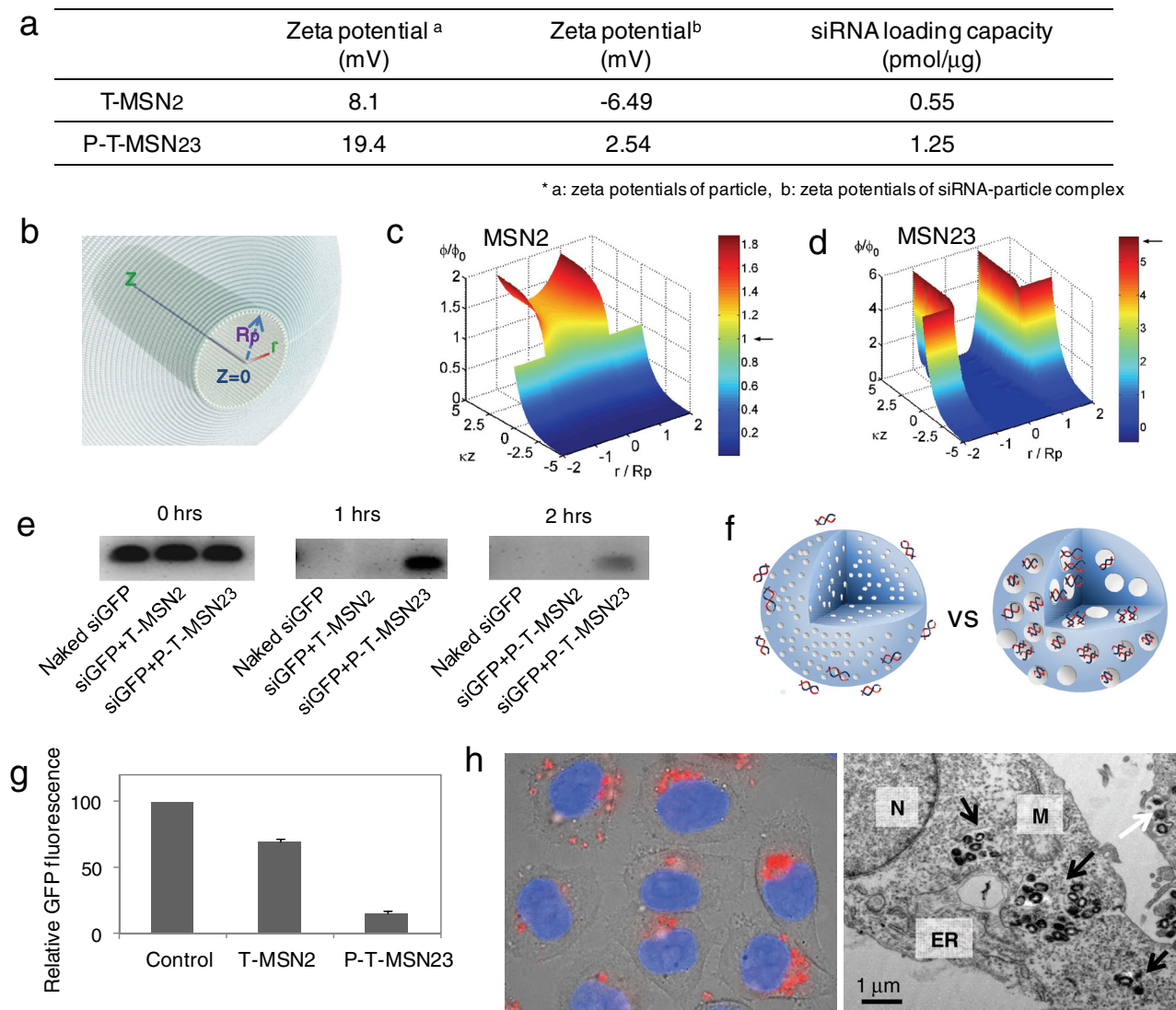


Figure 3. Complex formation of T-MSN2 and P-T-MSN23 with siRNA, electric potential near MSN pores, GFP knockdown efficiency, and cellular uptake of MSNs. a) Zeta potentials before and after siRNA loading onto MSNs were measured. The siRNA loading capacity of P-T-MSN23 is about twofold higher than that of T-MSN2. P-T-MSN2 showed very little loading of siRNA under the same conditions (data not shown). Therefore, T-MSN2, instead of P-T-MSN2, was used as a control for the particles with small pores. b) Illustration of the MSN geometry with a pore of radius R_p ; the z coordinate is along the pore axis and r measures the distance from the axis ($0 \leq r \leq R_p$). c,d) Electric potentials (ϕ) for MSNs with small ($R_p = 1.05$ nm, MSN2) (c) and large pores ($R_p = 11.5$ nm, MSN23) (d) are calculated assuming that positive charges are uniformly distributed both at the outer surface ($z = 0$) and the pore wall ($z > 0, r = R_p$) with charge density σ . The strength of the electric potential, scaled with ζ potential of MSN2 ($\approx \sigma(R_p = 1.05 \text{ nm})/\epsilon \kappa \phi_0$), is color-coded from blue to red. The arrows next to the color bars indicate the values of ϕ/ϕ_0 at the outer surface of the MSN, which are 1 and ≈ 5.49 (estimated) for MSN2 (c) and MSN23 (d), respectively. Note that the difference between electric potential (ϕ/ϕ_0) inside the pore ($z > 0$) and the outer surface ($z = 0$) is larger if the pore is smaller. e) siRNA protection assay from RNase: lane 1, naked siRNA; lane 2, siRNA–T-MSN2 complex; lane 3, siRNA–P-T-MSN23 complex. Data show that siRNA in the P-T-MSN23 complex is still intact even after incubation of the complex with RNase for 1 h at 37 °C. f) Loading of siRNA into P-T-MSN23 is most likely established inside the pore, but not in T-MSN2, due to differences in pore size. g) Relative GFP expressions were determined as 69 and 15% for T-MSN2 and P-T-MSN23, respectively, which indicates that P-T-MSN23 is a highly potent siRNA delivery vehicle. h) P-T-MSN23 were observed in the perinuclear region after cellular uptake. N: nucleus, M: mitochondria, ER: endoplasmic reticulum.

(Figure 3d). Even though the physicochemical calculation results suggest that the loading of siRNA inside the pores is favorable, we cannot completely exclude the possibility of adsorption of the siRNAs “onto” the MSN surface. However, it is most likely that the majority of siRNAs are loaded inside the pores even if some siRNAs are adsorbed onto the outer surface of the MSN.

We next evaluated the resistance of the siRNA–MSN complex against RNase-mediated degradation of siRNA and performed functional delivery of siGFP using both T-MSN2 and P-T-MSN23 in HeLa cells (cervical cancer cells) stably expressing GFP (Figure 3e). Protection of siRNA from nuclease is a key consideration for accomplishment of a clinically relevant siRNA delivery vehicle. The degree of siRNA

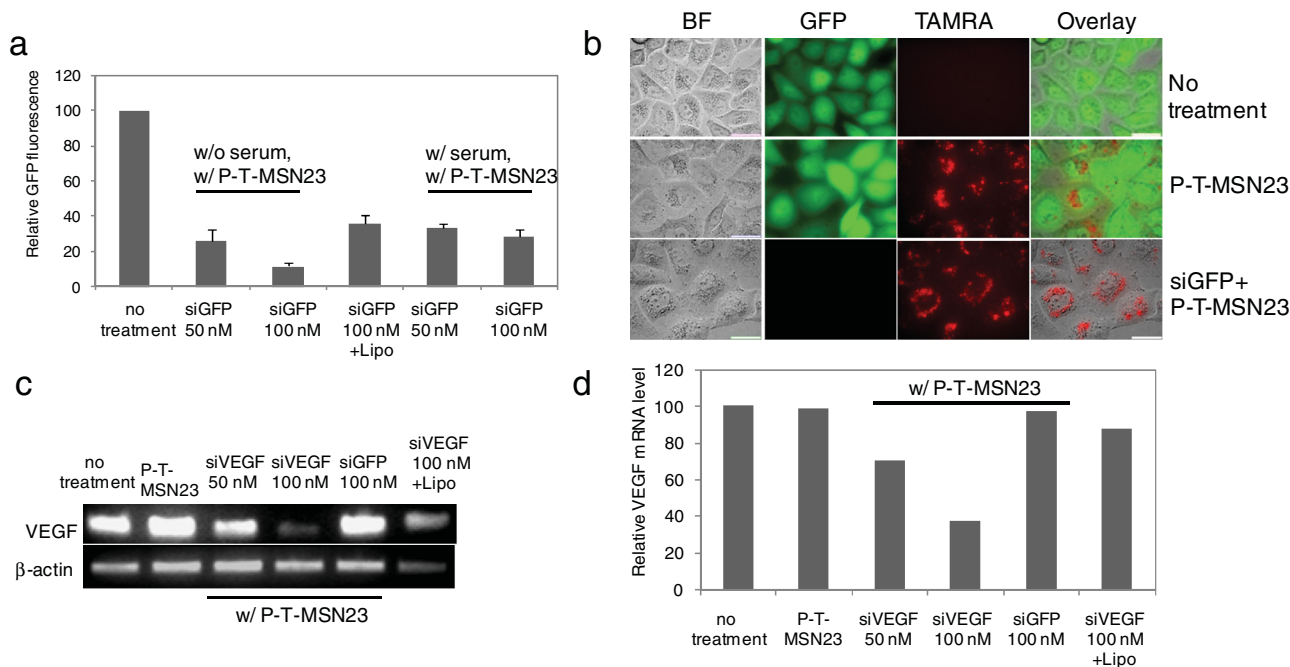


Figure 4. Knockdown of GFP and VEGF genes with P-T-MSN23 in vitro. a) GFP knockdown efficiency was measured by flow cytometry. Relative GFP expression was measured as 26% (50 nM siGFP–P-T-MSN23), 12% (100 nM siGFP–P-T-MSN23), 36% (siGFP–Lipofectamine), 33% (50 nM siGFP–P-T-MSN23 in the presence of serum), and 29% (100 nM siGFP–P-T-MSN23 in the presence of serum). b) Optical images of GFP HeLa after treatment of MSN23 and siGFP–P-T-MSN23 clearly shows the downregulation of the GFP gene in siGFP–P-T-MSN23-treated cells. BF = bright field. c, d) VEGF mRNA levels were analyzed by performing RT-PCR after incubation with MDA-MB-231 cells. Remarkable downregulation of VEGF mRNA was observed in siVEGF–P-T-MSN23-treated cells in a dose-dependent and sequence-specific manner.

degradation was determined by running a gel electrophoresis after incubation of siGFP–T-MSN2 and siGFP–P-T-MSN23 complexes, which were prepared by incubation of siGFP and the MSNs in a ratio of 1.25 pmol siRNA to 1 μ g MSNs in PBS, in the presence of RNase for 1 and 2 h at 37 $^{\circ}$ C, followed by heparin-mediated detachment of siRNA from the particles. The gel image in Figure 3e shows that siRNA loaded to P-T-MSN23 is still intact even after incubation of the complex with RNase for 1 h at 37 $^{\circ}$ C, whereas siRNA with T-MSN2 completely disappeared, which suggests that siRNAs might be loaded inside the pores in the case of P-T-MSN23, thus preventing access of RNase to siRNA, as depicted in Figure 3f. That being said, further incubation of siRNA–P-T-MSN23 with RNase for 2 h induced significant siRNA degradation, which might be attributed to slow but continuous dissociation of siRNA from pore walls as the incubation time increases, to reach equilibrium between bound and unbound states. In fact, the loaded siRNAs were completely released from the vehicle after incubation with heparin for 5 min (60 μ g of heparin was used for 10 μ g of siRNA–MSNs in 10 μ L PBS; data not shown).

Knockdown of GFP gene expression, as a model gene, was next carried out by addition of siRNA–MSN complexes (25 pmol siRNA with 20 μ g MSN in 250 μ L of serum-free medium, which is equivalent to 100 nM siRNA) to GFP-expressing HeLa cells that were seeded in a 24-well cell culture plate at a density of 2×10^4 cells per well 24 h prior to transfection (the optimum nucleic acid/particle ratio was determined as 1.25 pmol μ g $^{-1}$). The GFP expression level

was determined by flow cytometry after 48 h of incubation. Relative GFP expressions were measured as 69 and 15% for T-MSN2 and P-T-MSN23, respectively, based on mean fluorescence of GFP, thereby indicating that P-T-MSN23 is a much more potent siRNA delivery vehicle than T-MSN2 (Figure 3g). Fluorescence and TEM images showed the presence of internalized P-T-MSN23 in cytoplasm and, more specifically, their accumulation, mainly around the perinuclear region (Figure 3g,h). Since P-T-MSN23 is superior to T-MSN2 as a siRNA delivery vehicle according to the experimental data, we carried out all of the following experiments using P-T-MSN23.

We next examined the siRNA concentration dependency of gene silencing, the effect of serum proteins, and compared the degree of target gene downregulation mediated by P-T-MSN23 with that assisted by Lipofectamine 2000 (Figure 4a). The mean GFP gene expression level decreased to 26 and 12%, compared with control cells, upon treatment of 50 and 100 nM siGFP complexed with P-T-MSN23 in serum-deficient medium, respectively. Gene knockdown was achieved in a concentration-dependent manner, even in the presence of 10% serum, but with slightly less efficiency. It is notable that the efficacy of P-T-MSN23-assisted siGFP delivery, which inhibited GFP expression down to 12%, is even significantly higher than that of Lipofectamine-assisted siGFP delivery showing reduced gene expression down to 36%. Cellular uptake of P-T-MSN23 and the relative GFP expression levels were further confirmed by fluorescence microscope images, which showed little green fluorescence

in HeLa cells treated with siGFP–P-T-MSN23 complex, compared with control cells treated with P-T-MSN23 only, and perinuclear accumulation of particles, as presented in the red fluorescence originating from TAMRA dye conjugated to P-T-MSN23 (Figure 4b). Nanoparticle-based systems showing higher efficiency than Lipofectamine in siRNA-induced gene knockdown as a cellular delivery strategy have been reported by several research groups; however, most of the aforementioned nanoparticles were prepared by coating with cationic polymers, such as polyethyleneimine (PEI), which often shows notable cytotoxicity within a range of effective concentrations. However, our P-T-MSN23 showed no reduction in cell viability ($106 \pm 5.3\%$), even at a much higher concentration ($640 \mu\text{g mL}^{-1}$) than that typically used ($80 \mu\text{g mL}^{-1}$; see Figure S4). Our siRNA delivery system does not require any further surface modification for improvement of knockdown efficiency, since surface conjugation of cell-penetrating peptide (MPAP, myristoylated polyarginine peptide) to MSNs did not result in improvement of GFP gene silencing efficiency (Figure S5). Taken together, the present P-T-MSN23 affords a functional siRNA delivery vehicle based on inorganic nanoparticles, which accomplishes higher siRNA transfection efficiency than Lipofectamine without requiring a cationic polymer surface coating, while remaining noncytotoxic at effective concentrations and even well above the effective concentrations as well.

Next, we investigated downregulation of a therapeutically relevant gene, vascular endothelial growth factor (VEGF). VEGF is a signaling protein that plays a critical role in angiogenesis in rapidly growing tumors by activation of endothelial cells when it binds to the VEGF receptor (VEGFR).^[29] Due to its important role in tumor growth, efforts have been made to inhibit VEGF expression or function for reduction of angiogenesis in cancer therapy.^[30] VEGF downregulation was carried out with MDA-MB-231 cells, a breast cancer cell line, by incubation with complexes of P-T-MSN23 with siRNA against VEGF (siVEGF) at 50 and 100 nM. Dose-dependent reduction in VEGF expression (lane 3 (50 nM siVEGF) and lane 4 (100 nM siVEGF)) was revealed by reverse transcription polymerase chain reaction (RT-PCR) after 24 h of incubation, which semiquantitatively determined the VEGF mRNA level of each sample (Figure 4c,d). The VEGF mRNA level was downregulated only in cells treated with siVEGF (lanes 3 and 4, Figure 4c), not in cells treated with siGFP (100 nM, lane 5), thus indicating that degradation of VEGF mRNA was induced by siVEGF in a sequence-specific manner. The siVEGF–P-T-MSN23 complex induced VEGF gene silencing more effectively than in cells treated with siVEGF based on the Lipofectamine system, shown as a faint band (lane 4, siVEGF–P-T-MSN23, Figure 4c) and a bright band (lane 6, siVEGF–Lipofectamine) when the same concentrations of siVEGF were employed, which is consistent with the gene knockdown results of GFP.

We next demonstrated the applicability of our siRNA delivery system in vivo using xenografts of GFP-expressing HeLa and MDA-MB-231 cells. **Figure 5a** shows in vivo fluorescence images of mice bearing GFP-expressing HeLa xenografts before and after intratumoral injection of siGFP–P-T-MSN23 complex and PBS as a control. Decreased green

fluorescence intensity corresponding to GFP in the siGFP–P-T-MSN23-treated xenograft tumor, compared with the PBS treated one, is clearly demonstrated (Figure 5a). A decrease of fluorescence derived from GFP was also observed in the extracted tumors, showing reduction of fluorescence down to 42% (Figure 5b). Tissue slices prepared from xenograft tumors treated with P-T-MSN23 alone and siGFP–P-T-MSN23 complex were examined under a fluorescence microscope. Bright red fluorescence of TAMRA was observed in images of both tumor sections; however, green fluorescence originating from GFP was significantly reduced in the slice of tumor treated with siGFP–P-T-MSN23, thus indicating that P-T-MSN23-mediated functional siGFP delivery was accomplished in vivo and that GFP gene silencing was induced by siGFP in complex with P-T-MSN23, not by P-T-MSN23 itself (Figure 5c).

VEGF gene knockdown was next investigated with MDA-MB-231 xenografts in vivo. The first intratumoral injections were carried out when tumor volumes reached approximately 50 mm^3 . The siVEGF–P-T-MSN23 complex and controls, including PBS and naked siVEGF, were injected into each tumor four times (1 nmol of siVEGF at each injection) over a period of 20 days (at days 0, 5, 10, and 20) and tumor growth was monitored for 30 days from the initial injection. The tumor growth profile (Figure 5d) showed effective inhibition of tumor growth in the siVEGF–P-T-MSN23-treated tumor, compared with naked siVEGF or PBS-treated tumors. Weights of excised tumors treated with PBS, naked siVEGF, and siVEGF–P-T-MSN23 complex were measured as 240, 190, and 52 mg, respectively (see Figure S6 for images of tumor-bearing mice before extraction of tumors). VEGF mRNA levels were then measured by RT-PCR with extracted tumors after 30 days from the initial injection. Remarkable downregulation of VEGF mRNA was observed in tumors treated with siVEGF–P-T-MSN23 complex, compared with controls treated with PBS or naked siVEGF (Figure 5e).

To evaluate inhibition of blood vessel growth induced by siVEGF-mediated RNAi, we next performed immunohistochemistry using anti-CD31 antibody for visualization of blood vessels within tumor sections from an siRNA complex-treated xenograft. Fluorescence microscope images of the tumor sections indicated that siVEGF–P-T-MSN23 complex can suppress blood vessel growth, showing very weak staining of anti-CD31 antibody in the tumor treated with siVEGF–P-T-MSN23 complex, whereas control tumors exhibited bright fluorescence from anti-CD31 antibody (Figure 5f). Overall, our P-T-MSN23-based siRNA delivery system was effective in both a model gene, GFP, and a therapeutic target gene, VEGF, and the efficacy of siVEGF-mediated gene silencing was corroborated by RT-PCR results and inhibition of blood vessel growth in an in vivo xenograft model.

For the present study, the siRNA-loaded MSNs are intratumorally administered due to the aggregation tendency which prohibits intravenous administration. Therefore, for now, this MSN23 may find applications for tissues amenable to topical or localized therapy such as eye, skin, mucus membrane, and local tumors. Localized delivery has several benefits, including the potential for both higher bioavailability, given the proximity to the target tissue, and reduced adverse

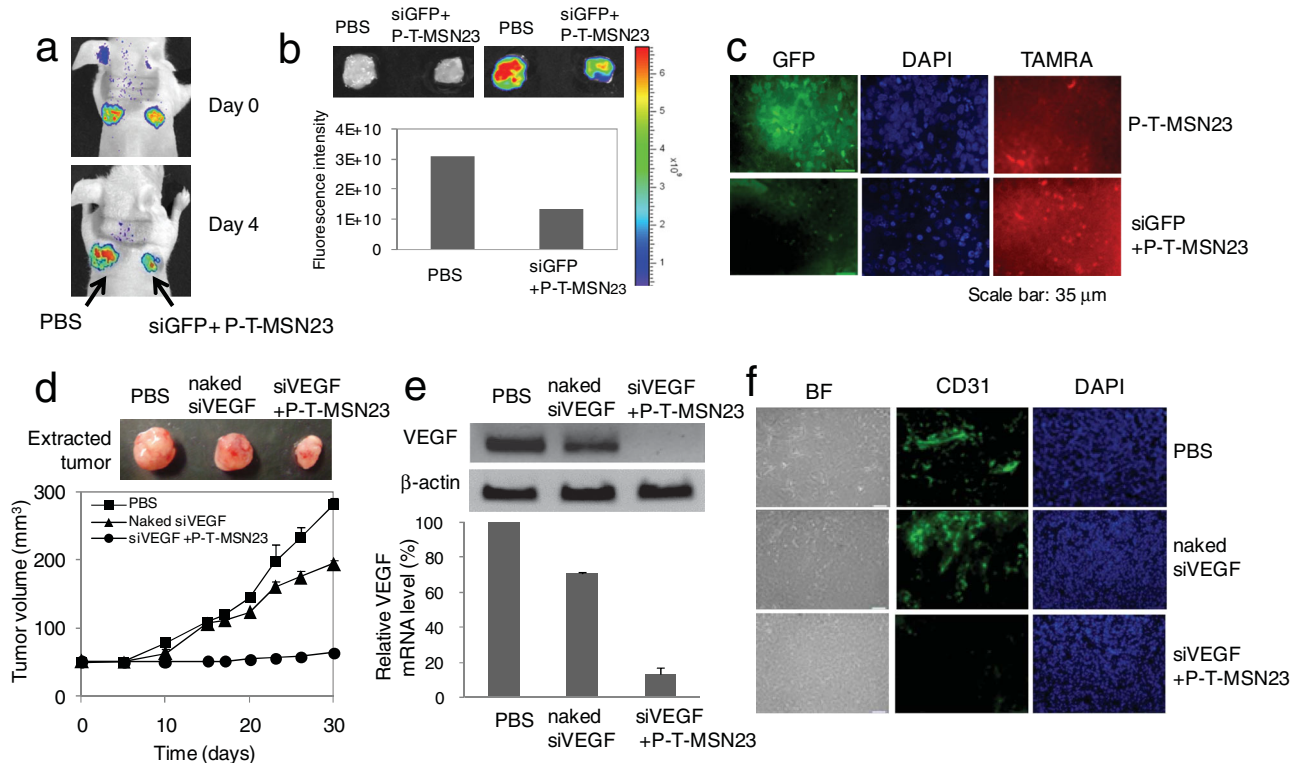


Figure 5. Knockdown of GFP and VEGF genes with P-T-MSN23 in vivo. a,b) In vivo optical images before (a) and after removal of tumors (b) and quantitative analysis of GFP-expressing tumors. c) Optical microscopic images of a tissue section after 4',6-diamidino-2-phenylindole (DAPI) staining show considerable reduction in GFP expression in the siGFP–P-T-MSN23-treated tumor, compared with tissue treated with P-T-MSN23. d) Tumor growth was observed for 30 days from the initial injections, which were performed when xenograft volumes reached approximately 50 mm³. Intratumoral injections of siVEGF–P-T-MSN complex, naked siVEGF, and PBS were performed four times at days 0, 5, 10, and 20. The tumor growth profile revealed no notable changes in tumor volumes when treated with siVEGF–P-T-MSN23 complex. Extracted tumors at day 30 are shown for size comparison. e) Significant downregulation of VEGF mRNA was observed in the siVEGF–P-T-MSN23-treated tumor, compared with the PBS- or naked siVEGF-treated tumor. Quantitative analysis of relative VEGF mRNA levels are presented as a bar graph. f) Inhibition of blood vessel growth in tumors treated with siVEGF–P-T-MSN23 was found by immunohistochemistry of tumor tissue sections with anti-CD31 antibody.

effects typically associated with systemic administration. Disease targets of local therapy are as follows: macular degeneration, atopic dermatitis, Huntington's disease, chronic pain, and glioblastoma multiforme.^[8]

3. Conclusion

We have demonstrated the ability of pore-expanded silica nanoparticles, P-T-MSN23, to deliver siRNA in vitro and in vivo, which showed remarkable downregulation of target genes, including the therapeutic gene VEGF. To date, MSNs have shown limited application in siRNA delivery due to their small pores. Our MSNs having ultralarge pores, \approx 23 nm in diameter, possess important advantages for functional and efficient siRNA delivery. First, siRNA delivery vehicle, P-T-MSN23, is prepared by a simple, cost-effective strategy with high monodispersity in a large quantity (more than 1 g per synthesis) in a short time. Second, in principle, any siRNA could be loaded onto P-T-MSN23 by simply mixing them in PBS and incubating for an hour, thus suggesting that the delivery system is modular. No chemical conjugation, crosslinker, or cumbersome purification/separation process is needed. The delivery vehicle may be prepared in a large quantity at

one time and used with appropriate siRNAs when needed. Third, siRNAs do not require laborious, expensive, and time-consuming chemical modifications, such as in locked nucleic acid (LNA) and *O*-methyl and phosphorothioate nucleic acids, to maintain chemical stability against nucleases since siRNAs are well protected by being loaded mostly inside pores of P-T-MSN23. Fourth, our delivery vehicle, P-T-MSN23 itself showed little cytotoxicity, even at high concentrations after amination. In addition, MSNs are generally considered biocompatible. With the simple system possessing all of these advantages, efficient and safe functional siRNA delivery was achieved in vitro and in vivo. Due to its high efficacy, biocompatibility, modularity, cost-effectiveness, and technical simplicity, the use of the present siRNA delivery strategy based on P-T-MSN23 could open the way to realization of exciting opportunities for use of RNAi in fundamental biology and biomedicine. We think that the present nanoparticle platform can be further improved by enhancing colloidal stability of the MSN23 and reducing the overall size of the MSN23 from 200 to around 100 nm, especially for therapeutic application. In addition, several important issues for gene silencing—when and where siRNA gets released from the particle inside

cells, how fast the siRNA release occurs, and how long gene silencing can be achieved—will be studied to enhance mechanistic understanding of the MSN23-mediated siRNA delivery and gene silencing in the near future.

4. Experimental Section

Synthesis of MSN2 and MSN23: Silica nanoparticles with 2 nm pores (MSN2) were prepared according to the literature, with little modification. In brief, cetyltrimethylammonium bromide (CTAB, 3.94 g) and 1 M NaOH solution (2.28 mL) were dissolved in methanol/water (800 g; 0.4:0.6, w/w). With vigorous stirring, tetramethoxysilane (TMOS, 1.3 mL) was added to the solution under ambient conditions. The reaction mixture was aged overnight after stirring for 8 h. The resulting white precipitate was purified for removal of remaining surfactant by centrifugation and washed with ethanol and water five times each. For preparation of MSN2, as-synthesized silica nanoparticles were suspended in ethanol (20 mL), followed by addition of HCl (4 mL). The suspension was refluxed overnight. The resulting white powder was isolated by filtration and washed with ethanol. For preparation of MSN23, as-synthesized silica nanoparticles were dispersed in ethanol by sonication for 30 min, followed by addition of water and TMB (20 mL of 1:1 mixture, v/v). The mixture was placed in an autoclave and kept at 140 °C for 4 days. The resulting white powder was washed with ethanol and water five times each. Organic surfactant was removed by refluxing in acidic ethanolic solution, as described above.

Preparation of Amine-Functionalized MSN2 and MSN23 and Conjugation of TAMRA: The template-extracted MSN2 and MSN23 (100 mg each) were suspended in toluene followed by the addition of APTES (1 mL). The suspension was refluxed overnight, filtered, and the residue washed with ethanol. Amine-grafted MSN2 and MSN23 (30 mg each) were suspended in dimethyl sulfoxide (DMSO, 1 mL) and *N*-hydroxysuccinimyl (NHS) ester-activated carboxytetramethylrhodamine (TAMRA-NHS) solution (10 μ L, 2.5 mg mL⁻¹ in DMSO) was added to the suspension. After stirring for 3 h, a pinkish powder was obtained by centrifugation and washing with ethanol and water five times.

PEGylation of MSN23: MeO-PEG-NH₂ (MW 5000 g mol⁻¹, Sunbio Inc.) was reacted with same amount of 3,3'-dithiodipropionic acid di(*N*-hydroxysuccinimide ester) overnight at room temperature. The reaction mixture was added to the suspension of T-MSN23 without purification, and stirred overnight at room temperature. The suspension was washed with ethanol and water five times. The resulting solid was dried under vacuum and dispersed in nuclease-free water.

Surface Characterization of MSN2 and MSN23: Nitrogen adsorption isotherms were measured in a NOVA sorption apparatus. Surface area calculations were carried out using the BET method and the pore size distribution was calculated according to the BJH method.

Cell Culture: HeLa (human cervical cancer cell line) cells, GFP-expressing HeLa cells, and MDA-MB-231 cells were cultured in Dulbecco's modified Eagle's medium (DMEM) containing D-glucose (4.5 g L⁻¹) and supplemented with 10% fetal bovine serum (FBS), penicillin (100 units mL⁻¹), and streptomycin (100 g mL⁻¹). Cells were maintained in a humidified incubator under 5% CO₂ at 37 °C.

Cellular Uptake Study: HeLa cells were seeded on a sterilized circular glass coverslip in a 24-well plate and cultured in an incubator. After 24 h, the cells were treated with P-T-MSN23 (80 μ g mL⁻¹) for 24 h, and then washed with PBS. For fixation, the glass coverslip with cells was immersed in 4% paraformaldehyde in PBS for 10 min at room temperature. Then, the cells on the coverslip were washed with PBS and mounted on a glass slide with nuclei staining by DAPI. Cell images were obtained using an inverted fluorescence microscope equipped with a 60 \times (1.4 numerical aperture) objective (Nikon Co., Japan) and a CoolSNAP cf charge-coupled device (CCD) camera (Photometrics, Tucson, AZ).

Gel Retardation Assay: To prepare each siRNA–nanoparticle complex, siRNA (100 pmol) was incubated with a predetermined amount of P-T-MSN23 at 4 °C in PBS. After 1 h of incubation, RNA loading dye was added to each mixture, and then the mixtures were loaded on the polyacrylamide gel. Gel electrophoresis was carried out at 90 V for 30 min in TBE (Tris/borate/EDTA) buffer, and the RNA bands were visualized on a UV trans-illuminator.

RNase Protection Assay: The siRNA–nanoparticle complexes were prepared to the final concentration of 25 pmol of siRNA against GFP (siGFP) with 20 μ g of particles in 5 μ L of PBS. The complexes were incubated for 1 h at room temperature. After adding RNase at a final 0.05% concentration, samples were incubated for varying times at 37 °C. The samples were treated with heparin and analyzed by polyacrylamide gel electrophoresis.

Cell Viability Test of MSNs: The cytotoxicity of P-T-MSN23 was tested by examining the viability of HeLa cells after the treatment of particles using the CCK-8 assay. HeLa cells were seeded in a 96-well cell culture plate 24 h before P-T-MSN23 treatment at a density of 1×10^4 cells per well. After incubation for 24 h, the cells were treated with varying concentrations of P-T-MSN23, and control cells were treated with equivalent volumes of PBS. After 24 h, the medium was removed, and serum-free medium (100 μ L) and CCK-8 solution (10 μ L) were added to each well. The cells were incubated for 1 h. The optical density of formazan salt at 450 nm wavelength was measured using a microplate reader (Molecular Devices, Inc., USA), and the background absorbance of the medium was subtracted. Experiments were carried out in triplicate, and data are shown as mean \pm standard error of the mean.

In vitro GFP Silencing: GFP HeLa cells were seeded in a 24-well cell culture plate at a density of 2×10^4 cells per well 24 h prior to transfection. GFP siRNA–particle complexes were prepared as follows. GFP siRNA (25 pmol) was incubated with P-T-MSN23 (20 μ g) in PBS at room temperature for 1 h. Each mixture (total volume 5 μ L) was then diluted with serum-free medium (245 μ L). GFP siRNA complexes in serum-free medium or serum-containing medium (250 μ L) were added to the cells and incubated for 8 h at 37 °C. Then the cells were washed with PBS and incubated for an additional 48 h in fresh serum-containing medium (500 μ L). Following incubation, knockdown and cellular uptake were investigated using a fluorescence microscope (Nikon Co., Japan). For quantification of knockdown efficacy, cells were washed with PBS, trypsinized, and then harvested. The samples were centrifuged at 4 °C and washed with cold PBS. After spinning down, cells were suspended in PBS containing 1% FBS and the suspension was filtered. Fluorescence intensity was measured using a FACSCalibur flow cytometer (Becton Dickinson, USA) equipped with an argon laser. Fluorescence intensity was shown as mean fluorescence of GFP.

In vitro VEGF Silencing: The level of VEGF mRNA was estimated by RT-PCR analysis. MDA-MB-231 cells were seeded in a 12-well cell culture plate at a density of 4×10^4 cells per well 24 h prior to transfection. Following incubation for 24 h, the medium was changed to serum-free DMEM and cells were treated with various nanoparticle complexes (5 μ L), including particles (80 μ g mL⁻¹) and 50 nm VEGF siRNA complex, 100 nm siRNA complex, 100 nm GFP siRNA complex, and 100 nm VEGF siRNA–Lipofectamine complex. Following incubation for 4 h, the medium was removed and replaced with serum-containing medium. Cells were trypsinized and harvested after incubation for 20 h. Total RNA was isolated using Trizol (Invitrogen, Carlsbad, CA) according to the manufacturer's protocol. RT-PCR was performed using a Super-Script II RT kit (Invitrogen, Carlsbad, CA). RT-PCR was carried out using the following thermal cycling conditions: cDNA synthesis; one cycle at 65 °C for 5 min, 42 °C for 2 min, 42 °C for 50 min, inactivation at 70 °C for 15 min, denaturation; one cycle 94 °C for 2 min, PCR amplification; 32 cycles at 94 °C for 20 s, at 60 °C for 30 s, and at 72 °C for 30 s, final extension; one cycle at 70 °C for 5 min. PCR primers for detection of human VEGF (forward, 5'-AGGAGGGCAGAATCATCACG-3'; reverse, 5'-CAAGGCCACAGGGATTCT-3') and human β -actin (forward, 5'-GCTCGTCGTCGACAACGGCTC-3'; reverse, 5'-CAAACATGATCTGGTCATCTCTT-3') were obtained from Genotech, Inc. (Daejeon, Korea). Sizes of PCR products for VEGF and human β -actin were 522 and 1153 bp (base pairs), respectively. PCR products were separated in a 0.8% agarose gel by electrophoresis.

In vivo GFP Silencing: All animal care and experimental procedures were approved by the Animal Care Committees of KAIST. For in vivo optical imaging, a xenograft tumor model was generated by subcutaneous injection of EGFP HeLa cells (2×10^6 cells per tumor) in PBS into the flank region of female nude mice. When the diameter of tumors reached around 5 mm, GFP siRNA complexed with P-T-MSN23 (1 nmol) in PBS was intratumorally injected twice (one injection per day). The control group was injected with same amount of particles in PBS omitting siRNA. After 4 days from final injection, the GFP expression of tumors was visualized by an IVIS Lumina imaging system (Xenogen, USA). The tumor tissue was removed and also visualized by the IVIS Lumina imaging system. The tissue was fixed, embedded in paraffin, cut off in 5 μ m thickness, and rehydrated. The tissue section was stained with DAPI and analyzed by using inverted fluorescence microscopy (Nikon Co., Japan).

In vivo VEGF Silencing: The xenograft tumor model was generated by subcutaneous injection of MDA-MB-231 cells (2×10^6 cells per tumor) in PBS into the flank region of female nude mice. When the volume of tumors reached around 50 mm³, VEGF siRNA complexed with P-T-MSN23 (1 nmol) in PBS was intratumorally injected at days 0, 5, 10, and 20. Control groups were injected with the same amounts of siRNA in PBS or only PBS. The tumor volume was determined by measuring the perpendicular diameters using the digital caliper to monitor the tumor growth tendency based on the formula: tumor volume = major axis \times (minor axis)² \times ($\pi/6$). After 30 days from initial injection, tumors were removed and visualized by an IVIS Lumina imaging system to confirm the presence of particles. The tissues were weighed and homogenized. To determine the intratumoral level of VEGF mRNA, total RNA was isolated from the tumor tissue using Trizol, according to the manufacturer's protocol. RT-PCR was performed with three tissues. The procedure was the same as described above. The tissue was fixed,

embedded in paraffin, cut off in 5 μ m thickness, and rehydrated. Antigen retrieval was carried out under heating conditions in citrate buffer and the tissue section was incubated with 1% bovine serum albumin (BSA) in PBS followed by the incubation of CD31 antibody. Finally, the sections were incubated with Alexa Fluor 488 goat anti-mouse antibody, washed, and mounted with DAPI. The sections were analyzed using an inverted fluorescence microscope equipped with a 60 \times (1.4 numerical aperture) objective (Nikon Co., Japan) and a CoolSNAP cf CCD camera (Photometrics, Tucson, AZ).

Supporting Information

Supporting Information is available from the Wiley Online Library or from the author.

Acknowledgements

This work was supported by the Basic Science Research Program through the National Research Foundation of Korea (NRF) funded by the Korean government (MEST) (Grant Nos. 313-2008-2-C00538, 2008-0062074, 2010-0000602, 2011-0017356, 2011-0020322) and by the Nano R&D program of NRF funded by MEST (2008-2004457) in Korea. R.R. acknowledges support from the National Honor Scientist Program (20100029665) and World Class University Program (R31-2010-000-10071-0) of the MEST in Korea. H.J. was partially supported by a GRL "Theragnosis" grant from the Korean Government (MEST) and thanks the Advanced Analysis Center in KIST (Korea Institute of Science & Technology) for use of TEM.

- [1] S. M. Elbashir, J. Harborth, W. Lendeckel, A. Yalcin, K. Weber, T. Tuschl, *Nature* **2001**, *411*, 494.
- [2] A. Fire, S. Xu, M. K. Montgomery, S. A. Kostas, S. E. Driver, C. C. Mello, *Nature* **1998**, *391*, 806.
- [3] A. J. Hamilton, D. C. Baulcombe, *Science* **1999**, *286*, 950.
- [4] Y. Dorsett, T. Tuschl, *Nat. Rev. Drug Discovery* **2004**, *3*, 318.
- [5] D. Bumcrot, M. Manoharan, V. Kotliansky, D. W. Y. Sah, *Nat. Chem. Biol.* **2006**, *2*, 711.
- [6] L. Gitlin, S. Karelsky, R. Andino, *Nature* **2002**, *418*, 430.
- [7] A. Ptasznik, Y. Nakata, A. Kalota, S. G. Emerson, A. M. Gewirtz, *Nat. Med.* **2004**, *10*, 1187.
- [8] K. A. Whitehead, R. Langer, D. G. Anderson, *Nat. Rev. Drug Discovery* **2009**, *8*, 129.
- [9] R. S. Tomar, H. Matta, P. M. Chaudhary, *Oncogene* **2003**, *22*, 5712.
- [10] H. Lee, S. I. Kim, D. Shin, Y. Yoon, T. H. Choi, G.-J. Cheon, M. Kim, *Biochem. Biophys. Res. Commun.* **2009**, *378*, 192.
- [11] J. Yano, K. Hirabayashi, S. Nakagawa, T. Yamaguchi, M. Nogawa, I. Kashimori, H. Naito, H. Kitagawa, K. Ishiyama, T. Ohgi, T. Irimura, *Clin. Cancer Res.* **2004**, *10*, 7721.
- [12] B. Urban-Klein, S. Werth, S. Abuharbeid, F. Czubayko, A. Aigner, *Gene Ther.* **2005**, *12*, 461.
- [13] A. M. Derfus, A. A. Chen, D.-H. Min, E. Ruoslahti, S. N. Bhatia, *Bioconjugate Chem.* **2007**, *18*, 1391.
- [14] J.-H. Lee, K. Lee, S. H. Moon, Y. Lee, T. G. Park, J. Cheon, *Angew. Chem.* **2009**, *121*, 4238; *Angew. Chem. Int. Ed.* **2009**, *48*, 4174.

- [15] T. Xia, M. Kovichich, M. Liong, H. Meng, S. Kabehie, S. George, J. I. Zink, A. E. Nel, *ACS Nano* **2009**, *3*, 3273.
- [16] H. Meng, M. Liong, T. Xia, Z. Li, Z. Ji, J. I. Zink, A. E. Nel, *ACS Nano* **2010**, *4*, 4539.
- [17] J.-S. Lee, J. J. Green, K. T. Love, J. Sunshine, R. Langer, D. G. Anderson, *Nano Lett.* **2009**, *9*, 2402.
- [18] H. Lv, S. Zhang, B. Wang, S. Cui, J. Yan, *J. Controlled Release* **2006**, *114*, 100.
- [19] J. Soutschek, A. Akinc, B. Bramlage, K. Charisse, R. Constien, M. Donoghue, S. Elbashir, A. Geick, P. Hadwiger, J. Harborth, M. John, V. Kesavan, G. Lavine, R. K. Pandey, T. Racie, K. G. Rajeev, I. Rohl, I. Toudjarska, G. Wang, S. Wuschko, D. Bumcrot, V. Koteliansky, S. Limmer, M. Manoharan, H.-P. Vornlocher, *Nature* **2004**, *432*, 173.
- [20] J. L. Vivero-Escoto, I. I. Slowing, B. G. Trewyn, V. S.-Y. Lin, *Small* **2010**, *6*, 1952.
- [21] J. L. Vivero-Escoto, I. I. Slowing, C. W. Wu, V. S.-Y. Lin, *J. Am. Chem. Soc.* **2009**, *131*, 3462.
- [22] E. Aznar, M. D. Marcos, R. Martinez-Manez, F. Sancenon, J. Soto, P. Amoros, C. Guillem, *J. Am. Chem. Soc.* **2009**, *131*, 6833.
- [23] K. Patel, S. Angelos, W. R. Dichtel, A. Coskun, Y.-W. Yang, J. I. Zink, J. F. Stoddart, *J. Am. Chem. Soc.* **2008**, *130*, 2382.
- [24] D. R. Radu, C.-Y. Lai, K. Jeftinija, E. W. Rowe, S. Jeftinija, V. S.-Y. Lin, *J. Am. Chem. Soc.* **2004**, *126*, 13216.
- [25] A. M. Chen, M. Zhang, D. Wei, D. Stueber, O. Taratula, T. Minko, H. He, *Small* **2009**, *5*, 2673.
- [26] F. Torney, B. G. Trewyn, V. S.-Y. Lin, K. Wang, *Nat. Nanotechnol.* **2007**, *2*, 295.
- [27] Recently, we demonstrated that the pore-expanded MSN enabled higher efficiency for plasmid DNA transfection than the conventionally used MSN with small pores. See, M.-H. Kim, H.-K. Na, Y.-K. Kim, S.-R. Ryoo, H. S. Cho, K. E. Lee, H. Jeon, R. Ryoo, D.-H. Min, *ACS Nano* **2011**, *5*, 3568.
- [28] K. Yano, Y. Fukushima, *J. Mater. Chem.* **2004**, *14*, 1579.
- [29] N. Ferrara, *Breast Cancer Res. Treat.* **1995**, *36*, 127.
- [30] Y. Takei, K. Kadomatsu, Y. Yuzawa, S. Matsuo, T. Muramatsu, *Cancer Res.* **2004**, *64*, 3365.

Received: January 5, 2012
Published online: